ADVANCED FUNCTIONAL MATERIALS
www.afm-journal.de

Hybrid Templated Synthesis of Crack-Free, Organized Mesoporous TiO_2 Electrodes for High Efficiency Solid-State Dye-Sensitized Solar Cells

*Jung Tae Park, Won Seok Chi, Dong Kyu Roh, Sung Hoon Ahn, and Jong Hak Kim**

Organic/inorganic hybrid templates, i.e., aluminium oxide (Al_2O_3) nanoparticles grafted with poly(oxyethylene) methacrylate, Al_2O_3-POEM, are synthesized via surface-initiated atom transfer radical polymerization (ATRP), as confirmed by Fourier transform-infrared spectroscopy (FT-IR) and thermogravimetric analysis (TGA). Upon combining the Al_2O_3-POEM with titanium(IV) isopropoxide (TTIP), hydrophilic TTIP is selectively confined in the hydrophilic POEM chains through hydrogen bonding interactions. Following the calcination at 450 °C and the selective etching of Al_2O_3 with NaOH, the OM-TiO_2 films with high surface areas, good interconnectivity, and anatase phase are obtained. The solid-state dye-sensitized solar cells (ssDSSCs) fabricated with OM-TiO_2 photoelectrodes and a polymerized ionic liquid (PIL) show a high energy conversion efficiency of 7.3% at 100 mW cm^{-2}, which is one of the highest values for ssDSSCs. The high cell performance is due to the well-organized structure, resulting in improved dye loading, excellent pore filling of electrolyte, enhanced light harvesting, and reduced charge recombination.

1. Introduction

In 1991, the Gratzel group reported their innovative work with a solar cell based on the photosensitization of dye adsorbed onto nanocrystalline TiO_2 films, i.e., a dye-sensitized solar cell (DSSC).[1] Since then, DSSCs have been considered a promising renewable photovoltaic technology due to their high power conversion efficiency, low cost, facile fabrication process and low manufacturing toxicity. Typically, DSSCs consist of a sensitizing dye, mesoporous TiO_2 photoelectrode, Pt-coated counter electrode and an electrolyte containing a redox couple, i.e., I^-/I_3^-. In order to improve cell performance, considerable attention has been directed toward developing sensitizing dyes,[2] TiO_2 photoelectrodes,[3–7] electrolytes,[8–10] and counter electrodes.[11,12] In particular, the TiO_2 photoelectrode is a very important element because sensitizer absorption, electron transport and recombination characteristics are directly influenced by TiO_2 properties such as crystallinity, phase, particle size, surface area, interconnection between particles and pore morphology.

A photoelectrode should have a high surface area and an organized structure with uniform pores, which facilitates dye loading, pore filtration of electrolytes and electron transfer. The most common technique for preparation of TiO_2 nanoparticles is the hydrolysis of a TiO_2 precursor with excess water catalyzed by acid or base, followed by hydrothermal growth and crystallization.[13,14] The produced nanoparticles are formulated in a paste with a binder and deposited onto transparent conducting oxide (TCO) substrates, which results in the randomly organized structures of TiO_2 film. Well-ordered arrays of vertically orientated TiO_2 nanotubes can be grown by potentiostatic anodization of Ti metal but the device is generally illuminated through the counter electrode, resulting in absorption losses from the counter electrode and the electrolyte.[15] Three-dimensionally, well-organized TiO_2 films can been prepared using a colloidal crystal template or holographic lithography method.[16–18] However, the surface areas of these TiO_2 films are not high enough to load a large amount of dye molecules, leading to a lower energy conversion efficiency. Block copolymer-templated synthetic strategies are also effective for generating well-defined organized TiO_2 films with large surface area and good interconnectivity.[6,7,19] However, the thickness of block copolymer-derived TiO_2 films is often limited to the submicron scale due to crack formation during calcination. Our group recently reported micron-thick organized TiO_2 films templated by a graft copolymer, i.e., poly(vinyl chloride)-g-poly(oxyethylene methacrylate) (PVC-g-POEM), using the addition of P25 nanoparticles[20] or the direct assembly of spindle-shaped, preformed TiO_2 nanoparticles.[21] Although these films were effective for solid state electrolytes with a large molecular volume, the thickness of the TiO_2 films that can be prepared was less than approximately 6 μm.

There has been much interest in fabricating solid-state DSSCs (ssDSSCs) due to the potential to decrease the overall weights of cells and provide long-term durability.[20–30] However, there have been only a few reported efficiencies greater than 7.0% at one sun condition.[21] Here we report a high

Dr. J. T. Park, W. S. Chi, D. K. Roh, S. H. Ahn,
Prof. J. H. Kim
Department of Chemical and Biomolecular Engineering
Yonsei University
262 Seongsanno, Seodaemun-gu,
Seoul 120-749, South Korea
E-mail: jonghak@yonsei.ac.kr

DOI: 10.1002/adfm.201200823

energy conversion efficiency of 7.3% at 100 mW cm^{-2}, which is one of the highest values for ssDSSCs. We describe a facile, effective method for preparing 10-μm-thick, crack-free, organized mesoporous TiO_2 (OM-TiO_2) films with good interconnectivity using hybrid templates, i.e., aluminium oxide (Al_2O_3) nanoparticles grafted with poly(oxyethylene) methacrylate, Al_2O_3-POEM. The resultant films were characterized in detail using Fourier transform-infrared spectroscopy (FT-IR), thermogravimetric analysis (TGA), X-ray diffraction (XRD), diffused reflectance spectroscopy, field-emission scanning electron microscope (FE-SEM) and Brunauer-Emmett-Teller (BET) analysis. The solid-state DSSCs (ssDSSCs) fabricated with OM-TiO_2 films and a polymerized ionic liquid (PIL) as a photoelectrode and a solid electrolyte, respectively, were characterized via current-voltage curves, incident photon-to-electron conversion efficiency (IPCE), intensity modulated photocurrent spectroscopy (IMPS)/intensity-modulated photovoltage spectroscopy (IMVS) and electrochemical impedance spectroscopy (EIS) measurements.

2. Results and Discussion

2.1. Preparation of OM-TiO_2 Films Using Hybrid Templates

Organic/inorganic hybrid templates were synthesized via a three-step synthetic approach involving surface-initiated atom transfer radical polymerization (ATRP), as illustrated in **Figure 1**. Step 1 involves the activation of hydroxyl (−OH) groups on the surface of Al_2O_3 nanoparticles. Step 2 consists of the conversion of −OH groups to −Cl groups using 4-(dimethylamino) pyridine (DMAP) under basic conditions. Finally, a hydrophilic polymer, i.e., POEM, was graft polymerized via ATRP using the Cl atom as an initiating site. The hybrid templates, i.e., Al_2O_3-POEM were used as a structure-directing agent to synthesize OM-TiO_2 photoelectrodes in three steps, as illustrated in **Figure 2**. Two kinds of Al_2O_3, with average diameters of approximately 13 nm and 50 nm, denoted as S-Al_2O_3 and L-Al_2O_3, respectively, were used to investigate the effect of nanoparticle size. Upon combining the Al_2O_3-POEM with a

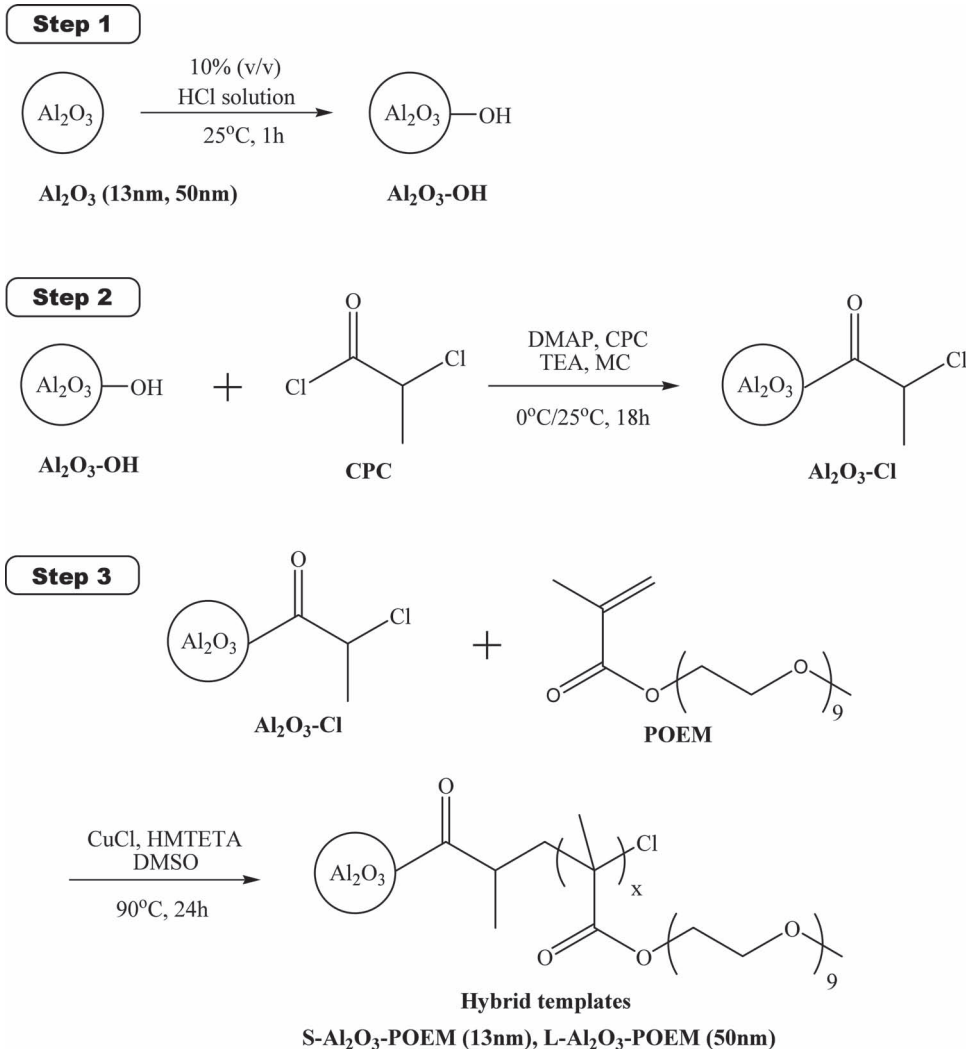

Figure 1. Procedures for the synthesis of hybrid templates, Al_2O_3-POEM.

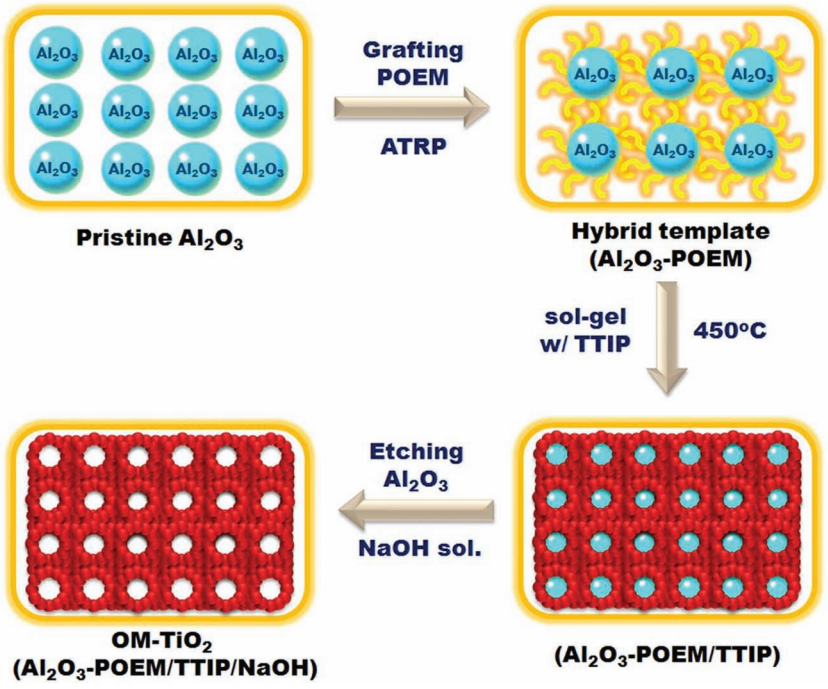

Figure 2. Schematic of the preparation of the OM-TiO_2 electrodes using hybrid templates.

TiO_2 precursor, titanium(IV) isopropoxide (TTIP), hydrophilic TTIP was selectively confined in the hydrophilic POEM chains through hydrogen bonding interactions. Following the sol-gel process and calcination at 450 °C, dense Al_2O_3-POEM/TTIP films were generated. The selective etching of Al_2O_3 with a 5 wt.% NaOH solution in water/methanol (8:2) for 12 h resulted in the formation of OM-TiO_2 films. It should be noted that a control sample, i.e. TiO_2 film prepared using unmodified Al_2O_3 nanoparticles as a template was not able to form micron-thick films with good mechanical properties due to the formation of macrocrack, as shown in Figure S1 (Supporting Information). This indicates that the strong interactions between the TTIP and the POEM grafted from Al_2O_3 are responsible for the formation of crack-free, OM-TiO_2 films.

The surface modification of the materials was confirmed using Fourier transform infrared (FT-IR) spectroscopy, as shown in Figure S2 (Supporting Information). None of the characteristic absorption peaks were visible for pristine S-Al_2O_3 (13 nm), with the exception of a broad band at 1000–600 cm^{-1}, attributable to the chemical bonding in alumina. Upon the activation of hydroxyl groups to produce S−Al_2O_3OH, the absorption bands of −OH stretching at 3392 cm^{-1} and H−O−H bending at 1645 cm^{-1} appeared. When the −OH groups were converted to −Cl groups (S−Al_2O_3Cl), additional peaks were observed at 1738 and 1448 cm^{-1} and 1402 cm^{-1}, attributable to the stretching vibration of C=O and to the bending vibration of −CH, respectively. A broad band at 3392 cm^{-1} assigned to the −OH stretching vibration was largely shifted to a lower wavenumber at 3123 cm^{-1} due to reduced hydrogen bonding interactions resulting from the conversion of −OH groups to −Cl groups. Following graft polymerization of POEM via ATRP (S-Al_2O_3-POEM), the strong peaks appeared at 1742 and 1102 cm^{-1}, assigned to the carbonyl (C=O) and the ether (C−O−C) stretching vibrations of POEM, respectively. Similar results were also obtained for the L-Al_2O_3 system, as shown in Figure S2b (Supporting Information). The thermogravimetric analysis (TGA) data in Figure S3 (Supporting Information) show that the grafting degree, i.e., the amount of POEM in the Al_2O_3 nanoparticles, was 22 and 26 wt.% for L-Al_2O_3-POEM and S-Al_2O_3-POEM, respectively. The slightly larger grafting degree of the S-Al_2O_3 nanoparticles arose from the large surface areas due to their small size (13 nm).

The structures and phase transitions of materials were also investigated using X-ray diffraction (XRD), as shown in Figure S4 (Supporting Information). Pristine S-Al_2O_3 (13 nm) and L-Al_2O_3 (50 nm) exhibited several peaks at 32.0, 36.4, 39.4, 45.4, 60.9 and 66.7, which correspond to the reflections from the (220), (311), (222), (400), (511) and (440) crystal planes of γ phase of alumina (JCPDS, Card No. 29-63). In S-Al_2O_3-POEM and L-Al_2O_3-POEM samples, a broad halo with weak intensity appeared at 19.2 and 20.8°, respectively, indicating the amorphous state of POEM.[31,32] Using the Bragg's law, the d-spacing values of POEM chains were calculated to be 4.6 and 4.3 Å for S-Al_2O_3-POEM and L-Al_2O_3-POEM, respectively. The slightly larger d-spacing of S-Al_2O_3-POEM represents that POEM polymeric chains are more densely packed in the S-Al_2O_3-POEM due to its larger grafting degree. The OM-TiO_2 films exhibited several sharp peaks at 25.6, 38.1, 48.4, 54.5, 63.1, and 69.7° correspond to the reflections from the (101), (004), (200), (105), (211) and (118) crystal planes of anatase TiO_2, respectively. It reveals that OM-TiO_2 films were in the purely anatase TiO_2 phase and the hybrid template Al_2O_3-POEM was completely removed by NaOH treatment and calcination at 450 °C.

2.2. Morphology and Structure of OM-TiO_2 Films

The morphological changes in the photoelectrodes were observed using field emission scanning electron microscopy (FE-SEM), as shown in **Figure 3**. Large, spherical nanoparticles with a 50 nm average diameter, few interconnections and large grain boundaries were observed in the pristine L-Al_2O_3 (Figure 3a). The L-Al_2O_3-POEM film had less porous structures due to pore filling of the POEM chains grafted from Al_2O_3 nanoparticles (Figure 3b). Upon combining with TTIP and calcination at 450 °C, a highly dense, compact structure without macro-cracks was obtained for the L-Al_2O_3-POEM/TTIP film (Figure 3c). This structure arose from the fact that TTIP, a Ti precursor, was selectively incorporated into the hydrophilic POEM chains of the hybrid templates (L-Al_2O_3-POEM) in which TiO_2 nanoparticles were formed in situ during a sol-gel process based on favorable interactions between TTIP and POEM. Upon selective etching with NaOH solution to dissolve the Al_2O_3

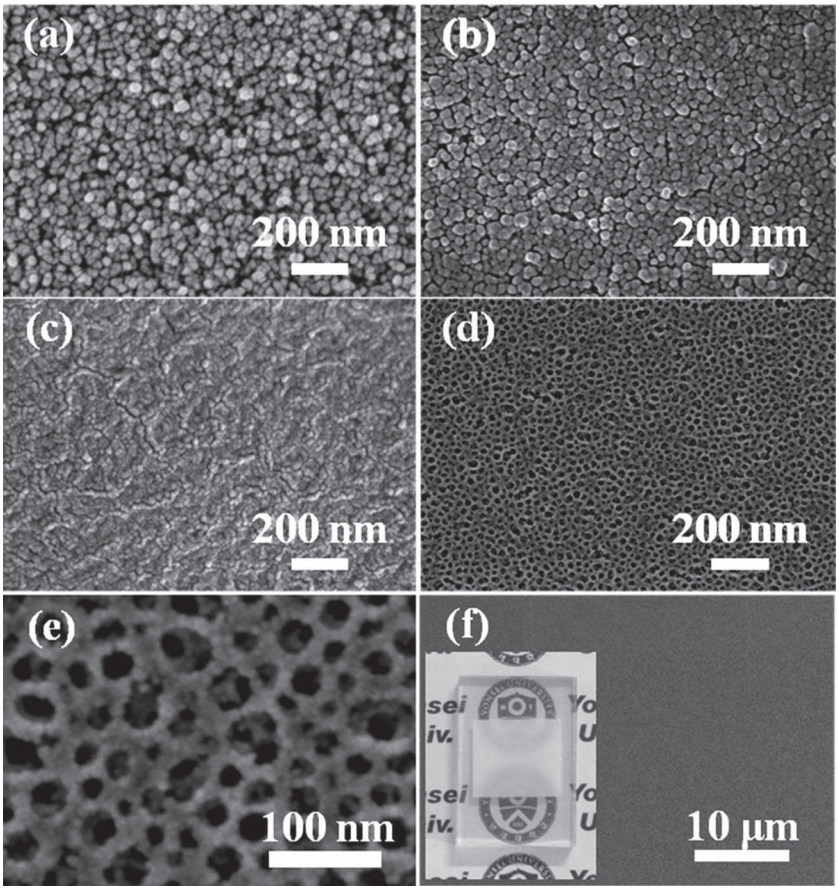

Figure 3. FE-SEM surface images of a) pristine L-Al_2O_3 (50 nm), b) L-Al_2O_3-POEM, c) L-Al_2O_3-POEM/TTIP, and d–f) OM-TiO_2 (L-Al_2O_3-POEM/TTIP/NaOH). The inset of (f) includes a photograph of OM-TiO_2.

nanoparticles, OM-TiO_2 photoelectrodes with high porosity and good interconnectivity were obtained with an average pore size of 61 nm (Figure 3d,e). This demonstrates that the hybrid templates (Al_2O_3-POEM) functioned as a robust and precise structure-directing agent. Similar results were obtained for the S-Al_2O_3 system, as shown in Figure S5 (Supporting Information). However, the overall porosity and pore size of OM-TiO_2 photoelectrodes prepared with S-Al_2O_3 were smaller than those with the L-Al_2O_3 system. This is because the same amount of Al_2O_3-POEM relative to TTIP was introduced for both systems for easier comparison. This result implies that the porosity can be enhanced by increasing the amount of S-Al_2O_3-POEM.

The organized structure of TiO_2 films was directly visualized in the FE-SEM cross-sectional images (**Figure 4**, Figure S6 (Supporting Information)), in which 10-μm-thick, crack-free TiO_2 films were observed. Interestingly, the overall porosity gradually decreased beginning at approximately 3 μm through the film thickness from the FTO substrate, leading to asymmetric structures with a gradient pore density. This is because the density of Al_2O_3 (1.06 g/mL) is lower than that of TiO_2 (3.0 g/mL) and thus the relative concentration of hybrid templates, Al_2O_3-POEM, is reduced near the FTO substrate, particularly from a thickness of 3 μm. Furthermore, the pore size was also reduced from approximately 61 to 38 nm and 18 to 14 nm for L-Al_2O_3-POEM and S-Al_2O_3-POEM, respectively, at thicknesses below 3 μm, which is presumably due to less aggregation in the hybrid template. Despite the reduced porosity and pore size near the FTO substrate, these asymmetric structures provide a basis for good adhesion properties between the TiO_2 and the FTO, resulting in reduced interfacial resistance and recombination loss. Since less porous TiO_2 films near the FTO maintain the entire structure, OM-TiO_2 films could be obtained without crack formation (Figure 3f, and Figure S4f (Supporting Information)).

2.3. Performances of ssDSSCs

The efficiency of DSSCs largely depends on the amount of dye loading, which is related, in turn, to the pore structure, connectivity, surface area and porosity of the TiO_2 films. Thus, the surface areas and pore volumes of the OM-TiO_2 films were determined by nitrogen adsorption-desorption as shown in Figure S7 (Supporting Information), and the results are summarized in **Table 1**. At higher pressures between 0.8 and 1.0 unit, the curves exhibited a hysteresis loop, indicating the presence of type IV mesopores. Specific surface area was calculated from nitrogen isotherms using the BET method, while average pore diameter was determined using the Barrett–Joyner–Halenda (BJH) method. The surface areas and pore volumes of the OM-TiO_2 films were always greater than those of P25, resulting in greater dye loading in the former. The surface area of the film prepared with S-Al_2O_3-POEM (90.1 m^2/g) was larger than that prepared with L-Al_2O_3-POEM (79.7 m^2/g), but the pore volume of the former (0.425 cm^2/g) was smaller than that of the latter (0.946 cm^2/g). This is because S-Al_2O_3-POEM generated small pores, resulting in a larger surface area and high dye loading. The pore distribution curve of L-Al_2O_3-POEM was quite narrow relative to P25, indicating the substantial homogeneity of the pores. These BET results show that the photoelectrodes fabricated with OM-TiO_2 films may generate more photoelectrons and enhance performance in DSSC. The performance of DSSC also strongly rely on the light scattering ability of the TiO_2 photoelectrode and thus the UV-visible reflectance spectra of the photoelectrodes were measured, as shown in Figure S8 (Supporting Information). The reflectance of the OM-TiO_2 films was always much larger than that of P25, indicating effective light scattering ability on the OM-TiO_2. The reflectance of the film prepared with L-Al_2O_3-POEM was slightly larger than that prepared with S-Al_2O_3-POEM, demonstrating that larger pores are more effective for light scattering.

The current density-voltage (J-V) curves of ssDSSCs fabricated using the 10-μm-thick OM-TiO_2 films as a photoelectrode were measured as shown in **Figure 5**a and the performances are summarized in Table 1. A PIL of

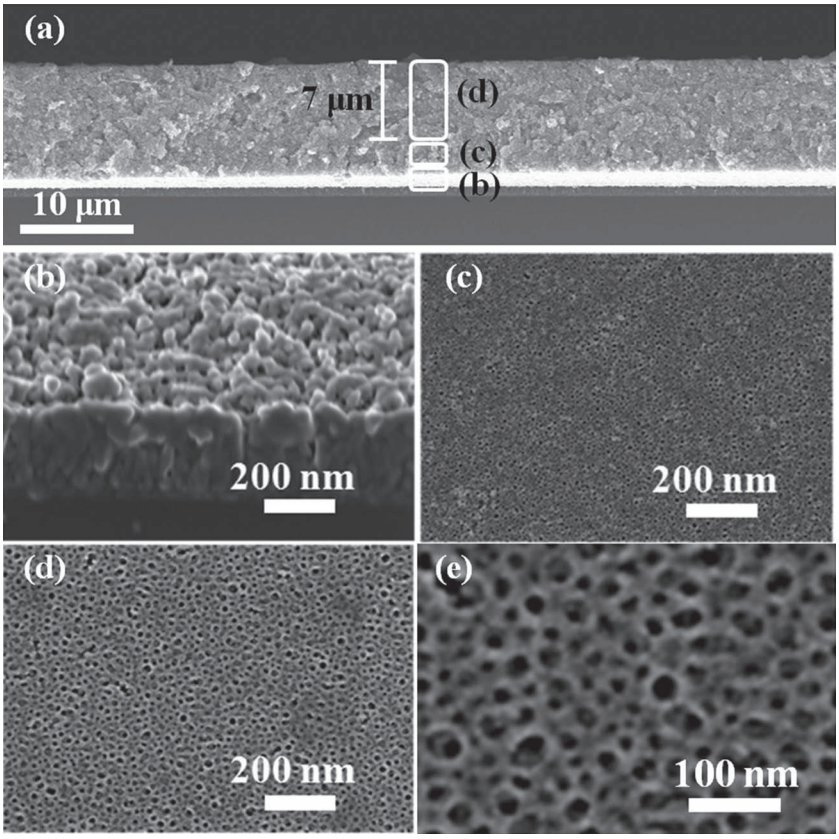

Figure 4. Cross-sectional FE-SEM images of OM-TiO_2 photoelectrodes (L-Al_2O_3-POEM/TTIP/NaOH): a) whole thickness, b) near the FTO substrate, c) lower 3-μm-thick regions, and d,e) upper 7-μm-thick regions.

poly((1-(4-ethenylphenyl)methyl)-3-butyl-imidazolium iodide) (PEBII) was employed as a solid electrolyte for the ssDSSC in which the incorporation of I_2 as an initial component of electrolyte was not necessary.[29] The conversion efficiency of the OM-TiO_2 prepared with S-Al_2O_3-POEM reached 7.3% at 100 mW/cm^2, which is one of the highest values observed for ssDSSCs[6–10,20–30] and approximately 1.7-fold greater than that of P25, indicating the importance of an organized structure. The efficiency improvement is due to three factors: improved dye adsorption, facilitated penetration of the solid electrolyte and increased electron transport. The increased short circuit current (J_{sc}) value is attributed to the higher accessible specific surface area in the OM-TiO_2 structure, enabling enhanced dye molecule loading. Higher cell performance in OM-TiO_2 also comes from the improved fill factor (FF) due to the facile and sufficient infiltration of solid electrolyte into the TiO_2 nanopores, as confirmed by cross-sectional FE-SEM image in Figure S9 (Supporting Information). There was also an increase in the open circuit voltage (V_{oc}) for OM-TiO_2 films, which results from the well-interconnected network structure of the TiO_2 layer, allowing increased electron transport and reduced interfacial charge recombination loss, which will be characterized by dark current and EIS analysis. The efficiencies of liquid electrolyte-based DSSCs with OM-TiO_2 films (Figure S10 (Supporting Information)) were only slightly larger than those of PEBII-based ssDSSCs, indicating more effectiveness in solid-state system.

The IPCE values of the ssDSSCs fabricated with OM-TiO_2 films and P25 are shown in Figure 5b as a function of illumination wavelength. The ssDSSCs with OM-TiO_2 films exhibited higher IPCE values than that with P25 over the whole spectral range, indicating effective utilization of light in the former. The IPCE value of S-Al_2O_3-POEM film was always larger than that of L-Al_2O_3-POEM at the wavelength region below 550 nm. However, the IPCE value of L-Al_2O_3-POEM was slightly greater than that of S-Al_2O_3-POEM film at the longer wavelength region of 550 ~ 700 nm, which results from the larger scattering effect in the former and consistent with the UV-visible reflectance spectra in Figure S8 (Supporting Information).

The electron transport and recombination kinetics of ssDSSCs were also investigated using EIS analysis as shown in Figure S11 (Supporting Information). The Nyquist plot generally features three semicircles that reflect the charge transfer resistance at the counter electrode in the kHz region, the Nernst-type impedance due to electron transport across the nanocrystalline titania layer and their recapture by tri-iodide in the Hz region and finally the so-called finite-Warburg impedance relative to the tri-iodide mass transport in the mHz region. However, the last semicircle was not clearly observed in Figure S11 (Supporting Information), implying a fast diffusion rate.[33] All spectra recorded were simulated and plotted using Z plot software with an equivalent circuit that depicts a general transmission line electrical model established originally to describe the macroscopic homogeneous porous electrode model. The frequency yielding the maximum of the imaginary impedance component of the large semicircle in the Nyquist plot corresponds to the inverse

Table 1. Surface area, amounts of adsorbed dye molecules and photovoltaic properties of ssDSSCs fabricated with three kinds of TiO_2 photoelectrodes and polymerized ionic liquid electrolyte at 100 mW/cm^2 (AM 1.5).

	Surface area [m^2/g]	Pore volume [cm^3/g]	dye adsorbed [nmol/cm^2]	V_{oc} [V]	J_{sc} [mA/cm^2]	FF	η [%]
P25	56.1	0.257	95.1	0.60	13.0	0.56	4.4
OM-TiO_2 (S-Al_2O_3-POEM)	90.1	0.425	149.7	0.75	16.2	0.60	7.3
OM-TiO_2 (L-Al_2O_3-POEM)	79.7	0.946	121.5	0.76	14.1	0.64	6.9

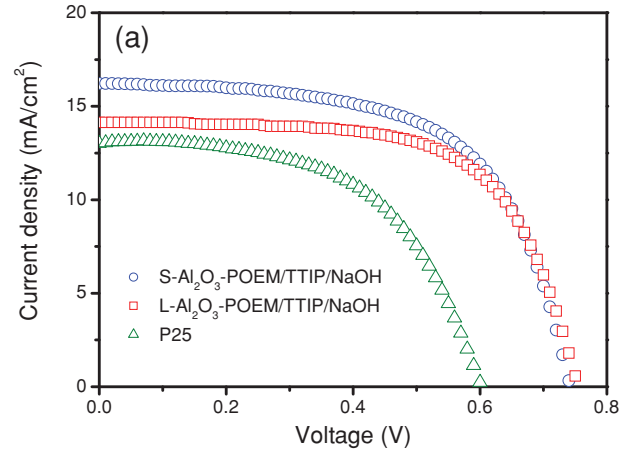

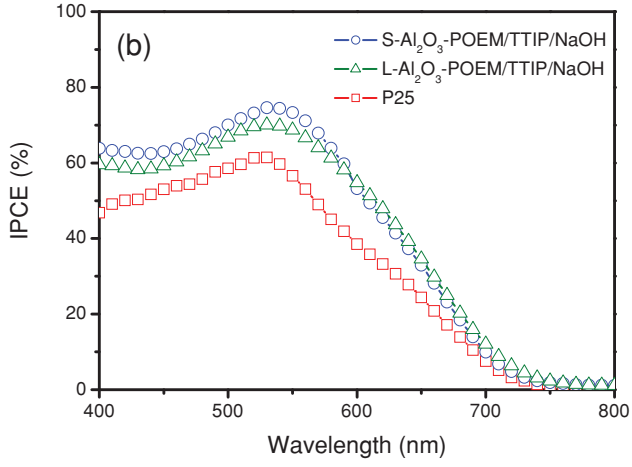

Figure 5. a) J–V curves and b) IPCE spectra of ssDSSCs fabricated with OM-TiO_2 films (S-Al_2O_3-POEM/TTIP/NaOH, L-Al_2O_3-POEM/TTIP/NaOH) and the P25 film at 100 mW/cm^2.

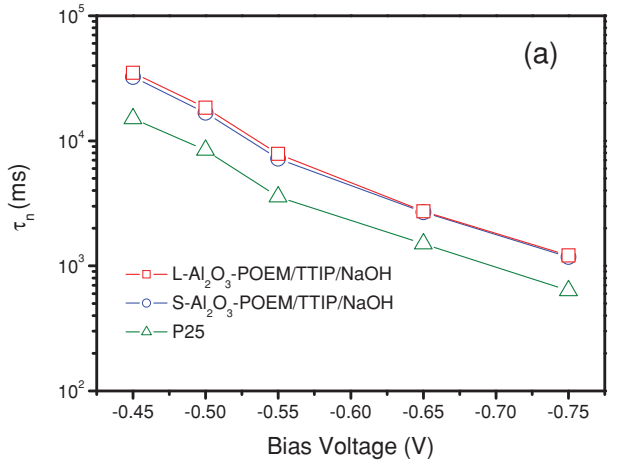

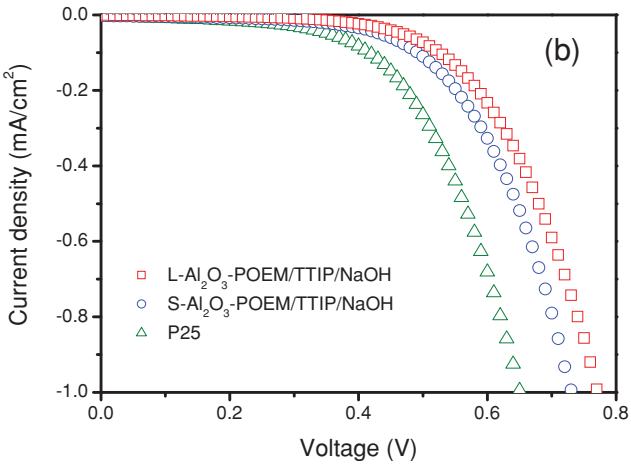

Figure 6. a) Electron lifetime (τ_n) and b) J–V curves in the dark for ssDSSCs fabricated with OM-TiO_2 films (S-Al_2O_3-POEM/TTIP/NaOH, L-Al_2O_3-POEM/TTIP/NaOH) and the P25 film.

relaxation time, which can in turn be interpreted as the electron lifetime or recombination time.[33] The logarithm of the recombination resistances (R_{rec}) and electron lifetime (τ_n) derived from the impedance data, are plotted in Figure S12 (Supporting Information) and **Figure 6**a, respectively, as a function of bias voltage. The electron lifetime (τ_n) was derived from the product between the resistance of recombination and the capacitance for the electron transfer. The logarithmic plots present the linear dependence of the electron lifetime as a function of the bias voltage for the different films. The larger recombination resistance and longer electron lifetime of OM-TiO_2 films were obtained, indicating suppressed recombination process. These results are attributable to the improved interfacial contact of the electrode/electrolyte due to the large pore size, pore volume and organized structure with good connectivity of the OM-TiO_2 films, as characterized by BET and SEM analysis. The lower dark current of OM-TiO_2 films also supports suppressed recombination, as shown in Figure 6b. The slightly longer electron lifetime of L-Al_2O_3-POEM film than S-Al_2O_3-POEM is presumably due to better connectivity of TiO_2 film with larger pore volume in the former. The IMPS/IMVS analysis also demonstrated that the electron diffusion coefficient and electron lifetime of OM-TiO_2 films were greater than that of P25 film, indicating an improved electron transport and reduced charge recombination of electrons in the former systems (Figure S13 (Supporting Information)). These OM-TiO_2 films could open new possibilities for the use of polymer electrolytes with large dimensions based on easier electrolyte infiltration into the pores and more efficient electron transfer, thereby reducing the corresponding recombination in ssDSSCs.

3. Conclusion

Crack free, 10-µm-thick, organized mesoporous TiO_2 films with high surface areas, good interconnectivity and uniform pores were prepared using an efficient hybrid template. An organic-inorganic hybrid template, i.e., Al_2O_3-POEM, is specially designed to improve the interfacial properties of films and for use as a structure-directing agent. The synthesis of hybrid templates and OM-TiO_2 films was confirmed by FT-IR,

TGA, XRD and FE-SEM analysis. The ssDSSCs fabricated with OM-TiO_2 photoelectrodes showed a high energy conversion efficiency of 7.3% and 6.9% at 100 mW cm^{-2} for 13 nm and 50 nm Al_2O_3, respectively, which are one of the highest values for ssDSSCs. The high efficiency is attributed to the well-organized TiO_2 structure with high surface areas and good interconnectivity, resulting in improved dye adsorption, excellent pore infiltration of solid polymer electrolyte and facilitated electron transfer, as confirmed by BET, IPCE, reflectance, IMPS/IMVS and EIS analysis. Furthermore, the pore size and porosity of TiO_2 films were controllable by changing the size of the Al_2O_3 or the grafting degree of POEM.

4. Experimental Section

Materials: Two types of Al_2O_3 nanoparticles (13 nm and 50 nm), hydrogen chloride solution (HCl), 2-chloropropionyl chloride (CPC, 97%), triethylamine (TEA, 99.5%), 4-(dimethylamino) pyridine (DMAP, 99%), poly(ethylene glycol) methyl ether methacrylate (POEM, $M_n \approx 475$ g/mol), copper(I) chloride (CuCl), 1,1,4,7,10,10-hexamethyltriethylene tetramine (HMTETA), titanium(IV) bis(ethyl acetoacetato) diisopropoxide, chloroplatinic acid hexahydrate (H_2PtCl_6), titanium(IV) isopropoxide (TTIP, 97%), sodium hydroxide solution (NaOH, 0.1 N), 1-butylimidazole, 4-chloromethylstyrene, lithium iodide (LiI), magnesium sulfate ($MgSO_4$) and 2,2′-azobisisobutyronitrile (AIBN) were purchased from Aldrich. Ruthenium dye (535-bisTBA, N719) was purchased from Solaronix, Switzerland. Methylene dichloride (MC, 99.8%), dimethyl sulfoxide (DMSO, 99.9%), acetonitrile (99.9%), butanol (99.9%), 2-propanol (99.9%), chloroform (99.9%), ethanol (99.9%), diethylether (99.9%) and ethyl acetate (99.9%) were purchased from J. T. Baker. Fluorine-doped tin oxide (FTO) conducting glass substrate (TEC8, 8 ohms/sq, 2.3-mm-thick) was purchased from Pilkington, France. All solvents and chemicals were reagent grade and were used as received without further purification.

Synthesis of Hybrid Templates (Al_2O_3-POEM): First, 10 g of Al_2O_3 nanoparticles (13 nm or 50 nm) were dispersed in 50 mL HCl (10% in H_2O) followed by stirring for 1 h to introduce the -OH groups onto the surface. The resulting Al_2O_3-OH was obtained by washing with water several times and evaporation of the solvent under vacuum. Second, 0.92 g of DMAP was mixed with 10 mL of methylene chloride (MC) and 0.7 mL triethylamine (TEA) in a 0 °C beaker with ice, followed by the addition of 1.2 mL 2-chloropropionyl chloride (CPC) in 10 mL MC. Then, 5.0 g of Al_2O_3-OH in 100 mL MC was added drop-wise to the solution, which was subsequently purged with N_2 for 30 min. The mixture was placed at room temperature for 18 h with continuous stirring. After the reaction, the resulting solution was precipitated into hexane, and the product was separated by centrifugation. The resulting Al_2O_3-Cl nanoparticles were dried in a drying oven at room temperature for 24 h and further dried in a vacuum oven for 24 h. Third, a hydrophilic polymer, POEM, was graft-polymerized via ATRP using Cl atoms as an initiating site. POEM (8 mL) was dissolved in 10 mL of DMSO. Then, 0.0264 g of CuCl and 0.072 mL of 1,1,4,7,10,10-hexamethyltriethylene tetramine (HMTETA) were added to the solution, followed by the addition of 2 g of the Al_2O_3-Cl nanoparticles. The solutions were purged with N_2 for 30 min and then placed in a 90 °C oil bath for 24 h. After polymerization, the resulting solution was precipitated into methanol to remove unreacted monomers, and the polymer was separated by centrifugation. Finally, hybrid templates, Al_2O_3-POEM, were obtained and dried in a vacuum oven overnight at room temperature.

Preparation of OM-TiO_2 Electrodes Using Hybrid Templates: First, the clean surface of FTO glass was coated with a layer of titanium(IV) bis(ethyl acetoacetato) diisopropoxide using spin coating, followed by calcination at 450 °C for 30 min. Then, the solutions consisting of Al_2O_3-POEM and TTIP were deposited onto the FTO glass using the doctor blade technique. The Al_2O_3-POEM/TTIP solutions were prepared as follows. TTIP (0.18 mL) was dissolved and stabilized in a 0.2 mL HCl solution containing 0.04 mL water with vigorous stirring. After aging for 15 min, the TTIP solution was added to 0.039 g of each Al_2O_3-POEM in a solution of 1.08 mL isopropanol, followed by mild stirring for 3 h at room temperature. After casting the Al_2O_3-POEM/TTIP solutions, the photoelectrodes were aged at room temperature under 80% relative humidity for 30 h and calcined at 450 °C for 30 min. After that, the Al_2O_3 nanoparticles in the photoelectrodes were dissolved using a 5 wt.% sodium hydroxide solution in water/methanol (8:2) at room temperature for 12 h.

Fabrication of the ssDSSCs: The DSSCs with an active area of 0.24 cm^2 were constructed by drop-casting of the polymer electrolyte solution onto the photoelectrode and covering with the counter electrode, following a previously reported procedure.[21,29] The TiO_2 photoelectrodes were sensitized with the 10^{-4} M ruthenium ((N-719) solution in ethanol at 50 °C for 4 h in a dark room. The Pt-coated counterelectrodes were prepared via spin-coating of a 7 mM H_2PtCl_6 solution in isopropyl alcohol and calcination at 450 °C for 30 min. The polymer electrolyte solutions in acetonitrile were directly cast onto the photoelectrode. Both electrodes were then superimposed and pressed between two glass plates to achieve slow evaporation of the solvent and a thin electrolyte layer. The cells were placed in a vacuum oven for 1 day for complete evaporation of the solvent.

Photoelectrochemical performances were measured using a Keithley Model 2400 and a 1000 W xenon lamp (Oriel, 91193). The light intensity was homogeneous over an 8×8 in^2 area, and its intensity was calibrated with a Si solar cell (Fraunhofer Institute for Solar Energy System, Mono-Si+KG filter, Certificate No. C-ISE269) for a sunlight intensity of one (100 mW/cm^2). IMPS/IMVS measurements were carried out on a electrochemical workstation equipped with a frequency response analyzer under a modulated red light emitting diode (635 nm) driven by a source supply, which can provide both DC and AC components of the illumination. The frequency range was set from 10000 Hz to 0.01 Hz. The IPCE spectra were measured as a function of wavelength from 400 to 800 nm (McScience, K3100).

Characterization: Fourier transform infrared (FT-IR) spectra of the samples were collected using an Excalibur Series FT-IR (DIGLAB Co.) instrument at frequencies ranging from 4000 cm^{-1} to 600 cm^{-1} at an ATR facility; 64 scans were signal-averaged at a resolution of 4 cm^{-1}. Thermogravimetric analysis (TGA) was performed using a Q-5000 (IR-TA Instruments, USA) from room temperature to 700 °C at a heating rate of 10 °C/min under a nitrogen atmosphere. The surface structures of electrodes were characterized by field emission scanning electron microscopy (FE-SEM) (SUPRA 55VP, NICEM, Carl Zeiss). X-ray diffraction (XRD) was performed on a Rigaku 18 kW rotating anode X-ray generator, with CuK_α radiation ($\lambda = 1.5406$ Å), operated at 40 kV and 300 mA. The 2θ range was from 5° to 60° with a scanning speed of 3°/min, and the distance from the sample to the detector was 185 mm. The specific surface area and specific pore volume of the TiO_2 films were measured at the N_2 adsorption-desorption isotherm via the Brunauer-Emmett-Teller (BET, for specific surface area) and Barrett-Joyner-Halenda (BJH, for specific pore volume) methods, using a Belsorp-mini II device, after drying of the sample at room temperature for one day in a vacuum oven. In advance of these measurements, the TiO_2 films were additionally degassed at 70 °C under dynamic vacuum (10^{-2} Torr) for 1 h.

Measurement of Dye Adsorption: First, the N719 dye-sensitized TiO_2 photoelectrode was dipped into 10.0 mL of a 10^{-2} M solution of NaOH in ethanol-H_2O (1:1). The mixture was stirred until complete desorption of the dye into the liquid occurred. The volume of the NaOH solution containing the fully desorbed dye was then measured by UV-visible spectroscopy. Amounts of the NaOH solutions were recorded, and the absorption value at 515 nm (as a function of wavelength) was used to calculate the number of adsorbed N719 dye molecules according to the Beer-Lambert law, $A = \varepsilon lc$, where A is the absorbance of the UV-visible spectra at 515 nm, $\varepsilon = 14{,}100$/M cm is the molar extinction coefficient of the dye at 515 nm, l is the path length of the light beam, and c is the dye concentration.

Supporting Information

Supporting Information is available from the Wiley Online Library or from the author.

Acknowledgements

The authors acknowledge the financial support of grant from the National Research Foundation (NRF) funded by the Korean government (MEST) through No.2012R1A2A2A02011268, the Korea CCS R&D Center, and the Korea Center for Artificial Photosynthesis (KCAP) (NRF-2011-C1AAA001-2011-0030278).

Received: March 23, 2012
Revised: June 20, 2012
Published online: July 20, 2012

[1] B. O'Regan, M. Gratzel, *Nature* **1991**, *353*, 737.
[2] C.-Y. Chen, S.-J. Wu, C.-G. Wu, J.-G. Chen, K.-C. Ho, *Angew. Chem., Int. Ed.* **2006**, *45*, 5822.
[3] D. Chen, F. Huang, Y.-B. Cheng, R. A. Caruso, *Adv. Mater.* **2009**, *21*, 2206.
[4] F. Zhuge, J. Qiu, X. Li, X. Gao, X. Gan, W. Yu, *Adv. Mater.* **2011**, *23*, 1330.
[5] P. A. Sedach, T. J. Gordon, S. Y. Sayed, T. Fürstenhaupt, R. Sui, T. Baumgartner, C. P. Berlinguette, *J. Mater. Chem.* **2010**, *20*, 5063.
[6] P. Docampo, S. Guldin, M. Stefik, P. Tiwana, M. C. Orilall, S. Huttner, H. Sai, U. Wiesner, U. Steiner, H. J. Snaith, *Adv. Funct. Mater.* **2010**, *20*, 1787.
[7] M. Nedelcu, S. Guldin, M. C. Orilall, J. Lee, S. Huttner, E. J. W. Crossland, S. C. Warren, C. Ducati, P. R. Laity, D. Eder, U. Wiesner, U. Steiner, H. J. Snaith, *J. Mater. Chem.* **2010**, *20*, 1261.
[8] C. P. Lee, P. Y. Chen, R. Vittal, K. C. Ho, *J. Mater. Chem.* **2010**, *20*, 2356.
[9] K. J. Jiang, K. Manseki, Y. H. Yu, N. Masaki, K. Suzuki, Y. L. Song, S. Yanagida, *Adv. Funct. Mater.* **2009**, *19*, 2481.
[10] X. Liu, W. Zhang, S. Uchida, L. P. Cai, B. Liu, S. Ramakrishna, *Adv. Mater.* **2010**, *22*, E150.
[11] Q. Tai, B. Chen, F. Guo, S. Xu, H. Hu, B. Sebo, X.-Z. Zhao, *ACS Nano* **2011**, *5*, 3795.
[12] J. D. Roy-Mayhew, D. J. Bozym, C. Punckt, I. A. Aksay, *ACS Nano* **2010**, *4*, 6203.
[13] A. Hagfeldt, G. Boschloo, L. Sun, L. Kloo, H. Pettersson, *Chem. Rev.* **2010**, *110*, 6595.
[14] F. Huang, D. Chen, X. L. Zhang, R. A. Caruso, Y.-B. Cheng, *Adv. Funct. Mater.* **2010**, *20*, 1301.
[15] K. Shankar, G. K. Mor, H. E. Prakasam, S. Yoriya, M. Paulose, O. K. Varghese, C. A. Grimes, *Nanotechnology* **2007**, *18*, 065707.
[16] E. S. Kwak, W. Lee, N.-G. Park, J. Kim, H. Lee, *Adv. Funct. Mater.* **2009**, *19*, 1093.
[17] C. T. Yip, H. Huang, L. Zhou, K. Xie, Y. Wang, T. Feng, J. Li, W. Y. Tam, *Adv. Mater.* **2011**, *23*, 5624.
[18] C.-Y. Cho, J. H. Moon, *Adv. Mater.* **2011**, *23*, 2971.
[19] M. Zukalova, A. Zukal, L. Kavan, M. K. Nazeeruddin, P. Liska, M. Gratzel, *Nano Lett.* **2005**, *5*, 1789.
[20] S. H. Ahn, J. T. Park, J. K. Koh, D. K. Roh, J. H. Kim, *Chem. Commun.* **2011**, *47*, 5882.
[21] S. H. Ahn, W. S. Chi, J. T. Park, J. K. Koh, D. K. Roh, J. H. Kim, *Adv. Mater.* **2012**, *24*, 519.
[22] J. Zhao, X. J. Shen, F. Yan, L. H. Qiu, S. T. Lee, B. Q. Sun, *J. Mater. Chem.* **2011**, *21*, 7326.
[23] G. Q. Wang, L. A. Wang, S. P. Zhuo, S. B. Fang, Y. A. Lin, *Chem. Commun.* **2011**, *47*, 2700.
[24] W. Zhang, Y. Cheng, X. Yin, B. Liu, *Macromol. Chem. Phys.* **2011**, *212*, 15.
[25] A. Abrusci, I-K. Ding, M. Al-Hashimi, T. Segal-Peretz, M. D. McGehee, M. Heeney, G. L. Freyd, H. J. Snaith, *Energy Environ. Sci.* **2011**, *4*, 3051.
[26] M. D. Brown, T. Suteewong, R. S. S. Kumar, V. D'Innocenzo, A. Petrozza, M. Lee, U. Wiesner, Henry J. Snaith, *Nano Lett.* **2011**, *11*, 438.
[27] S. Nejati, K. K. S. Lau, *Nano Lett.* **2011**, *11*, 419.
[28] S. Yanagida, Y. Yu, K. Manseki, *Acc. Chem. Res.* **2009**, *42*, 1827.
[29] W. S. Chi, J. K. Koh, S. H. Ahn, J. -S. Shin, H. Ahn, D. Y. Ryu, J. H. Kim, *Electrochem. Commun.* **2011**, *13*, 1349.
[30] J. K. Koh, J. Kim, B. Kim, J. H. Kim, E. Kim, *Adv. Mater.* **2011**, *23*, 1641.
[31] E. Perez, G. Todorova, M. Krasteva, J. M. Perena, A. Bello, M. M. Marugan, M. Shlouf, *Macromol. Chem. Phys.* **2003**, *204*, 1791.
[32] C. Álvarez, A. E. Lozano, J. de Abajo, J. G. de la Campa, M. J. Capitán, T. A. Ezquerra, *J. Chem. Phys.* **2004**, *120*, 8815.
[33] F. Sauvage, J.-D. Decoppet, M. Zhang, S. M. Zakeeruddin, P. Comte, M. Nazeeruddin, P. Wang, M. Gratzel, *J. Am. Chem. Soc.* **2011**, *133*, 9304.